ADVANCED FUNCTIONAL MATERIALS
www.afm-journal.de

Orientation Control of Metal–Organic Framework Membranes Through Magnetic Induced Room-Temperature Growth

Fujun Li, Zeyu Cao, Hui Zhang, Feichao Wu, Weijuan Guo, Yanqing Yang, Jingde Li, Xiongfu Zhang,* and Yi Liu**

Precise orientation regulation represents an important pathway for microstructure optimization and performance enhancement of metal–organic framework (MOF) membranes, which remains challenging to achieve. In this study, a magnetic field is employed to prepare Co-based zeolitic imidazolate framework-L (Co-ZIF-L) membranes with controlled orientation. The application of a magnetic field promotes the ordered migration of Co^{2+} ions along the magnetic field lines and enables Co^{2+} ions to orderly coordinate with ligands along the easy magnetization axis of MOF crystals, exposing the lowest energy crystal plane and promoting selective growth of MOF crystals. Resulting (200)-oriented Co-ZIF-L membrane with a thickness of ≈40 nm exhibits H_2/CH_4 separation factor of 59.1 with H_2 permeance of 2275 GPU. This work provides a facile and efficient strategy to accurately regulate the preferred orientation of MOF membranes toward superior gas separation.

1. Introduction

Membrane separation features low energy consumption, simple operation, and low carbon emission, showing great potential compared with conventional distillation and adsorption separation.[1] Metal–organic framework (MOF), constructed by metal ions/clusters coordinating to organic linkers, has emerged as a superb membrane candidate due to its regular pore size and adjustable framework topology.[2,3] Past decades witnessed enormous efforts to fabricate MOF membranes for H_2 purification,[4] CO_2 capture,[5] olefin/paraffin separation,[6,7] pervaporation,[8] and battery application.[9] Among various microstructural factors, orientation regulation can optimize transport path of gas molecules and reduce grain boundary defects in the MOF membranes, which is attributed to the reduced probability of intergranular defect formation due to the oriented growth of MOF crystals.[10,11] It is well recognized that orientation results in improved grain boundaries and optimal gas diffusion, thereby concurrently enhancing gas permeance and selectivity in comparison with their randomly oriented counterparts.[12,13] Therefore, fabricating highly oriented MOF membranes represents an effective protocol to achieve superior separation performance.

Employing metal precursor template and secondary growth have been widely adopted to prepare oriented MOF membranes.[14,15] To achieve higher degree of preferred orientation, deposition of highly oriented seed layers as well as precise control of the orientation of metal precursor is required, which greatly increases the difficulty in preparing oriented MOF membranes.[16] Simultaneously, current preparation methods can enable the fabrication of MOF membranes with specific orientation, making it difficult to achieve deliberate and precise control over membrane orientation toward target separations. Additionally, traditional methods for preparing oriented MOF membranes usually require high-temperature and high-pressure synthesis conditions. This undoubtedly increases energy consumption and preparation costs, accompanied by safety hazards.

External fields, like electric and magnetic fields, have been commonly employed to prepare functional nanostructures.[17] Magnetic fields can provide directional forces for the assembly of magnetic nanomaterials, thereby altering the microstructure of materials.[18] Metal ions, represented by Co^{2+} ions and Ni^{2+} ions, undergo directional migration in solutions guided by magnetic force, followed by deposition or coordination along the direction that reduces the surface energy of crystals.[19,20] 1D nanostructures[21,22] and oriented crystal materials[23–25] can be obtained in this way. Therefore, magnetic field has become an effective method for the preparation of oriented nanomaterials in energy-related fields.[26,27] However, to the best of our knowledge, currently, there remain no reports on the fabrication of highly oriented MOF membranes under a magnetic field, even though

F. Li, Z. Cao, H. Zhang, F. Wu, W. Guo, Y. Yang, J. Li
Hebei Provincial Key Laboratory of Green Chemical Technology and High Efficient Energy Saving, Tianjin Key Laboratory of Chemical Process Safety, School of Chemical Engineering and Technology
Hebei University of Technology
Tianjin 300130, China
E-mail: wufeichao321@hebut.edu.cn

X. Zhang, Y. Liu
State Key Laboratory of Fine Chemicals, School of Chemical Engineering, Dalian Key Laboratory of Membrane Materials and Membrane Processes
Dalian University of Technology
Dalian 116024, China
E-mail: xfzhang@dlut.edu.cn; diligenliu@dlut.edu.cn

The ORCID identification number(s) for the author(s) of this article can be found under https://doi.org/10.1002/adfm.202525582

DOI: 10.1002/adfm.202525582

Co, Ni and other magnetic metals have been commonly served as metal centers of MOF materials.

Cobalt-based zeolitic imidazolate framework-L (Co-ZIF-L) consists of periodic lamina alignment along the (200)-direction, accompanied by free linkers between laminae.[28,29] Co-ZIF-L exhibits two mass-transfer pathways, covering hexagon window-like apertures (≈0.34 nm) in one layer and galleries (≈0.40 nm) without free ligands between layers,[30,31] which makes it superb candidate for precise orientation control of MOF membranes. Additionally, the framework of Co-ZIF-L is more rigid compared with its isostructural Zn-ZIF-L as the Co—N bond is shorter and stiffer than the Zn—N bond,[32,33] making it more suitable candidate for membrane-based separation, although previous studies showed that its direct preparation is very difficult due to fast growth kinetics.

In this work, an external magnetic field is employed for preparing Co-ZIF-L membranes with tailorable orientation. Magnetic field facilitates an ordered movement of Co^{2+} ions, promoting their coordination with organic ligands along the (200) crystal plane of Co-ZIF-L grains with reduced surface free energy. Our results indicate that the preferred orientation of Co-ZIF-L membranes can be arbitrarily manipulated through regulating the direction of the magnetic field. Of particular note, (200)-oriented Co-ZIF-L membrane fabricated under parallel magnetic field possesses an ultrathin thickness of ≈40 nm, showing unprecedented H_2/CH_4 performance. It is expected that this strategy could serve as a powerful tool to tailor the preferred orientation of MOF membranes toward superior separations.

2. Results and Discussion

Figure 1a illustrates the procedure for magnetic field-assisted preparation of Co-ZIF-L membranes with different orientations. Different magnetic field angles were achieved by rotating the AAO substrates along the vertical *z*-axis (Figure S1, Supporting Information), which would generate Co^{2+} ion currents that present different angles with the substrate. The generated magnetic force guides the ordered migration of Co^{2+} ions and their coordination orientation with organic ligands to expose the crystal surface with the lowest surface energy, inducing the selective growth of the MOF crystals in the membranes. Therefore, MOF membranes with different orientations could be obtained with changed incidence angles of the magnetic field.

Figure 1b–h show the scanning electron microscope (SEM) images of MOF membranes achieved with magnetic-field angles of 0°, 15°, 30°, 45°, 60°, 75°, and 90°, respectively. Continuous MOF membranes were obtained at all the incidence angles of the magnetic field. Nonetheless, the obtained membranes present obvious differences in morphology and membrane thickness. These discrepancies may be attributed to the different deposition and growth processes of MOF crystals with the function of the magnetic field possessing diverse incidence angles. Different magnetic field angles would create different Co^{2+} ion flows that present different angles from the AAO surface, which result in different nucleation and growth processes of MOF crystals. Additionally, the membrane thickness gradually increases with the enhancement of angles between the magnetic field line and the support, as shown in Figure 1i. The membrane thickness is as low as 42 nm when a parallel magnetic field with an angle of 0° is applied, while the value is enhanced to 565 nm in the case of a 90° magnetic field angle, namely a vertical magnetic field. On the whole, the thicknesses of these membranes is relatively thinner compared with most of the reported MOF membranes, which is significant for simultaneous enhancement of gas permeance and selectivity.

In general, the morphological change of MOF membranes often stems from variation in the growth orientation of MOF crystals.[34] Thus, X-ray diffractometer (XRD) characterization is performed to explore whether it is applicable to as-prepared Co-ZIF-L membranes. The intensities of characteristic peaks of the (200) plane gradually increase with increasing angles from 0° to 90° (**Figure** 2a), while an opposite trend is observed for the characteristic peaks of the (020) plane. Additionally, highly *c*-axis and *b*-axis oriented MOF membranes could be achieved at angles of 0° and 90°, respectively, which correspond to preferred (200) and (020) orientations, respectively.[35,36] Besides, the XRD patterns for AAO discs are not obvious, consistent with some reports on AAO-supported MOF membranes.[37–39] The Orientation Index (OI) has been widely used for assessing the orientation of membranes, which indicates their crystal phase.[40] The calculated OI values are shown in Figure 2b, which intuitively display the variation of characteristic peak intensities under different magnetic fields. Specifically, the magnetic field angle of 0° results in the formation of (200)-oriented membranes, while (020)-oriented membranes are obtained at a magnetic field angle of 90°. Besides, the (020) characteristic peaks in the XRD patterns of the obtained MOF membranes strengthen with the increasing magnetic field angles, with the (200) peaks weakening. These results indicate that the change in growth orientation is responsible for the difference in morphology and thickness of these MOF membranes. Co-ZIF-L grains exhibit a unique 2D leaf-like structure (Figure S2, Supporting Information). The (200)-oriented membrane prepared at a magnetic field angle of 0° composes of MOF crystals spreading flat on the substrate, which exhibits the lowest membrane thickness. By contrast, the 90° produced (020)-oriented membrane contains MOF crystals vertically arranged on the AAO surface, showing the highest thickness. While MOF grains in the partially oriented membranes are located obliquely on the AAO surface, presenting centered membrane thicknesses compared with that of (200)- and (020)-oriented membranes. When the magnetic field angles increase, more (020) crystal plane is exposed compared to the substrate, leading to the thickness increase in the resulting membranes. From magnetic field angles of 0° to 90°, it is like the process of leaf-shaped MOF crystals standing up vertically, as shown in Figure 2c.

Figure S3 (Supporting Information) displays that the fourier transform infrared (FT-IR) spectra of Co-ZIF-L membranes prepared under different incidence angles for magnetic field are basically consistent, but the peaks for C=N show a trend of moving toward higher wave numbers from 0° to 90°, which may be due to the change in growth orientation of MOF crystals.[41] Subsequently, (200)-oriented MOF membrane was selected to perform X-ray photoelectron spectroscopy (XPS) characterization. The full spectrum in Figure S4a (Supporting Information) confirms the Co, N and C elements in the MOF material. The Co 2p spectrum presents two peaks at 780.7 and 796.4 eV (Figure S4b, Supporting Information), stemming from the Co $2p_{3/2}$ and Co $2p_{1/2}$ of Co^{2+}, respectively.[42] In the N 1s spectrum, the peaks for

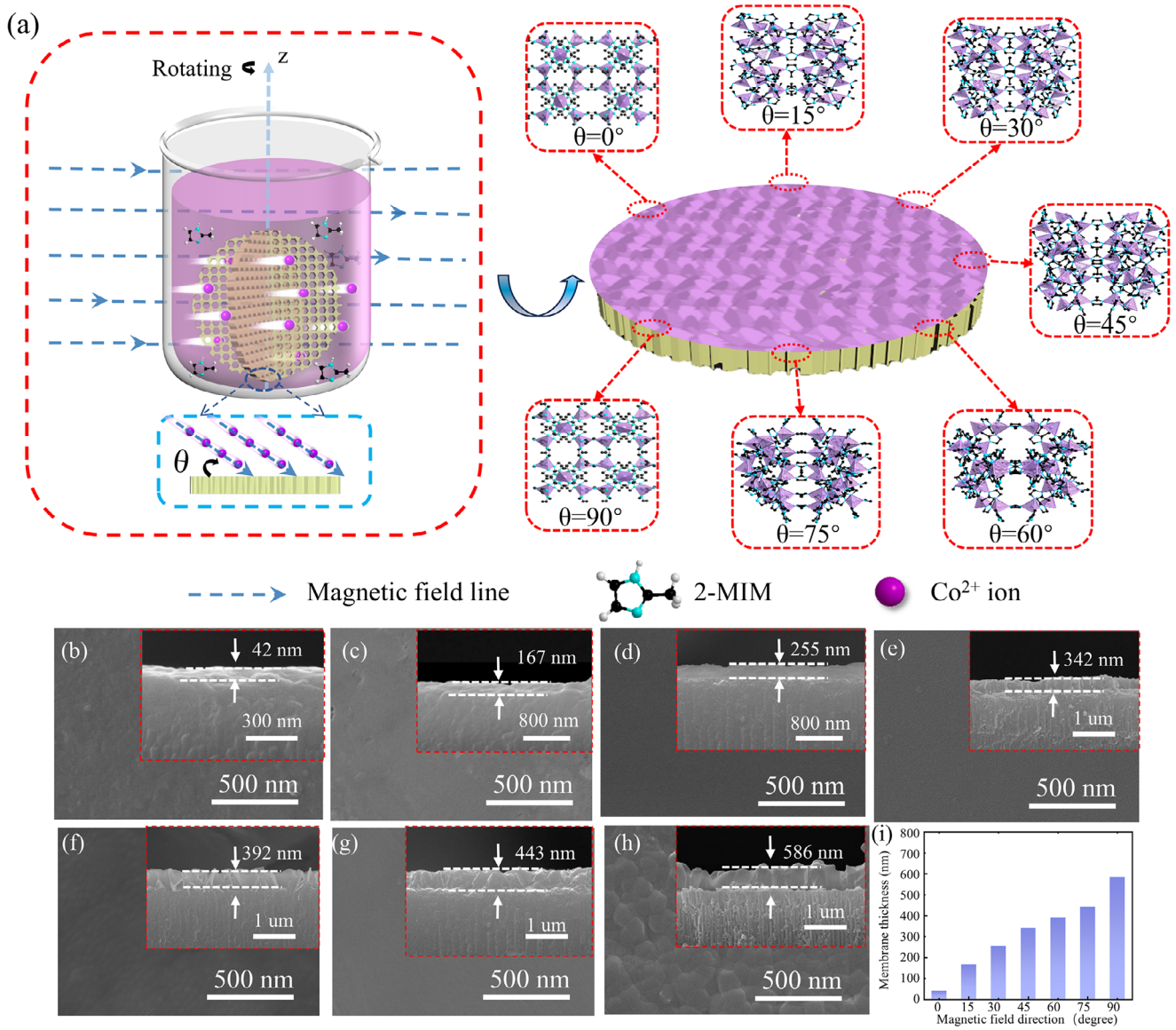

Figure 1. a) Schematic illustration of the preparation of Co-ZIF-L membranes with different orientations using the magnetic field assistance method. SEM images of Co-ZIF-L membranes prepared under the incidence angles for magnetic field: b) 0°, c) 15°, d) 30°, e) 45°, f) 60°, g) 75°and h) 90°. i) Thicknesses of different membranes.

Pyrrolic N, Co—N, and Pyridinic N are located at 405.1, 399.8, and 398.4 eV (Figure S4c, Supporting Information), respectively.[43] While the four peaks in Figure S4d (Supporting Information) at 292.7, 285.4, and 284.4 eV are attributed to the C═N, C—N, and C—H bonds, respectively.

Figures S5–S11 (Supporting Information) show SEM images of MOF membranes obtained under incidence angles of 0°, 15°, 30°, 45°, 60°, 75°, and 90° with different magnetic field intensities. It is observed that the optimized magnetic field intensity is the same (80 mT) with changed incidence angles, even though the morphologies of the obtained MOF membranes are different. Based on these results, we speculate that the directed motion of Co^{2+} ions by the action of the magnetic force is a reason for obtaining these oriented Co-ZIF-L membranes. Magnetic field would advacne the movement of metal ions along the magnetic field lines, and drive the transformation of electrons of Co from low to high spin states, thereby generating more unpaired electrons and magnetic moments to drive crystal plane rotation for reducing the system energy.[44,45] This facilitates the movement and sedimentation of metal ions along the easy magnetization direction to minimize system energy due to the magnetic anisotropy of the crystals.[46–48] Therefore, crystal planes with lower surface energy tend to be along the magnetic field lines during material synthesis under a magnetic field.[49] Besides, the crystal orientation can be easily regulated by changing the magnetic field direction,[50] consistent with the observations in this work. Therefore, we speculate that the formation of oriented Co-ZIF-L membranes followed a similar mechanism. Figure S12

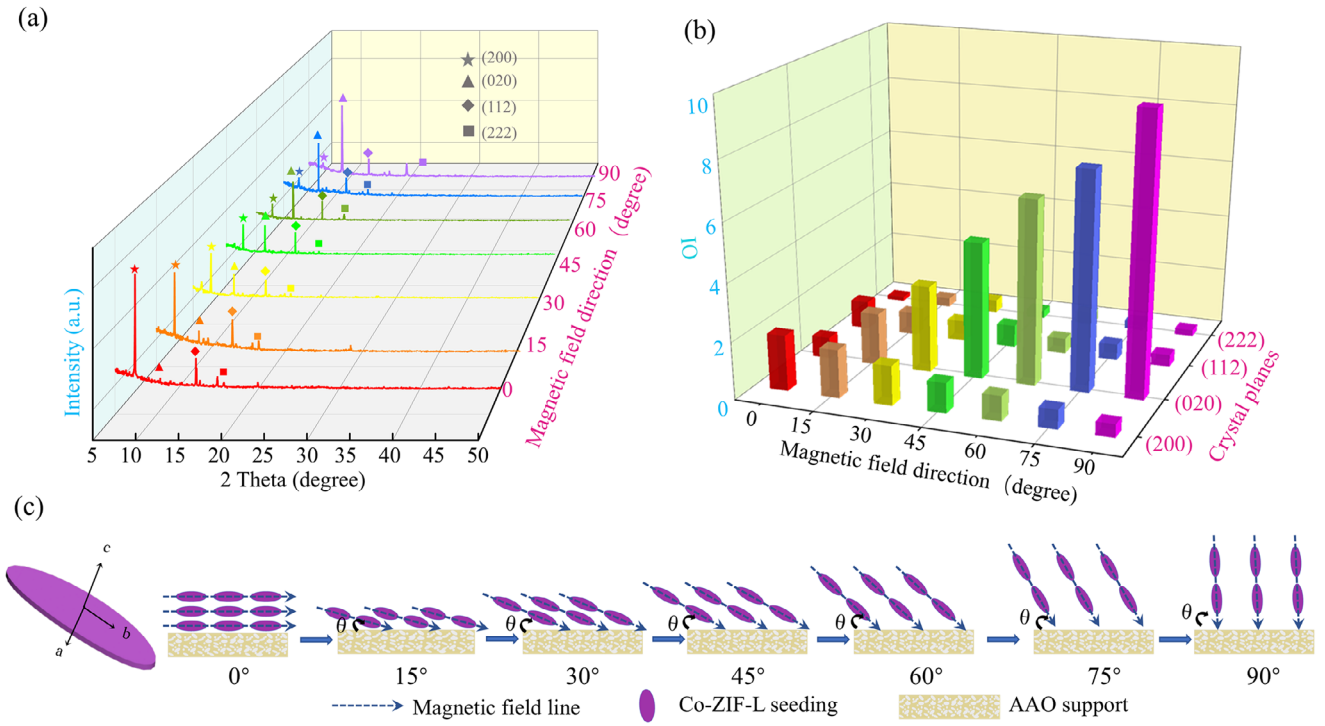

Figure 2. a) XRD patterns and b) the corresponding OI values, and c) the schematic showing of the possible mode for the formation of Co-ZIF-L membranes prepared under different magnetic fields.

(Supporting Information) compares Co 2p spectra of Co-ZIF-L grains synthesized under magnetic field and non-magnetic field conditions. Through integrating, we find that the Co^{3+}/Co^{2+} ratio in the Co-ZIL-L prepared under a magnetic field is higher than that of the conventional one, in which Co^{3+} corresponds to a high-spin state with Co^{2+} referring to a low-spin state.[51,52] This indicates that more high-spin Co has been created under a magnetic field. Then, the conductivity of Co^{2+} solutions under magnetic fields with different intensities was tested (Figure S13a, Supporting Information), based on which the corresponding migration rates of Co^{2+} ions can be achieved. Clearly, the enhancement of magnetic intensity accelerates the movement rate of Co^{2+} ions, as displayed in Figure S13b (Supporting Information). In a constant magnetic field, the paramagnetic Co^{2+} ions migrate directionally and acceleratedly along magnetic field lines under the magnetic force, which is in agreement with our previous results.[53] By contrast, Zn-ZIF-L membranes cannot be prepared under magnetic fields with different angles (Figure S14, Supporting Information), due to the weak effect of magnetic force on the non-magnetic Zn^{2+} ions. Additionally, increasing synthesis temperatures also leads to the failure of preparing dense Co-ZIF-L membranes (Figure S15, Supporting Information). As the increased temperature would accelerate the random movement and diffusion of ions, diminishing the magnetically-driven ion transport.[54]

Subsequently, the surface energy of the main crystal planes was estimated with the Materials Studio (MS) software. **Figure 3a** shows optimized models of the four main planes of the Co-ZIF-L crystal in the MS simulation (Figure S16, Supporting Information). The energy of (200) crystal facet is the lowest, while the energy for the (020) and (112) facets is very close, consistent with the density functional theory (DFT) result (Figure S17, Supporting Information) and the literature report.[55] This result indicates that (200) crystal facet possesses higher stability compared with other planes.[56] According to magnetic field theory, (200) direction (*c*-axis) is the easy magnetization axis of the Co-ZIF-L crystal.[57] When MOF synthesis is conducted in a magnetic field, the Co^{2+} would always be aligned and coordinated along the (200) direction. In other words, the magnetic field lines always run parallel with the (200) crystal plane. From the energy perspective, the applied magnetic field brings additional energy to the reaction system. Therefore, it tends to synthesize the crystal plane with the lowest surface energy to reduce the total system energy.

To verify the above points, we prepared Co-ZIL-L grains under different magnetic field strengths (Figure S18, Supporting Information). Figure S19 (Supporting Information) shows the XRD patterns of these samples. The OI value for (200) facet gradually increases with enhanced magnetic strength with an opposite trend for that of (020) facet (Figure 3b), agreeing well with our speculation. The XPS spectra of Co-ZIF-L powder prepared under different magnetic fields are shown in Figure 3c. The peak for the Co—N bond shifts toward lower energy with increasing magnetic intensity, indicating that the MOF crystal faces are regulated to reduce the system energy.[58] In terms of Raman spectra, vibrations located at 259, 311, and 429 cm^{-1} gradually increase with enhanced magnetic strength during processing (Figure 3d), implying the change in crystal orientation of the obtained MOF crystals.[58] Figure S20 (Supporting Information) shows that Co-ZIL-L membranes, prepared with different magnetic field angles, exhibit different hysteresis loops, indicating the

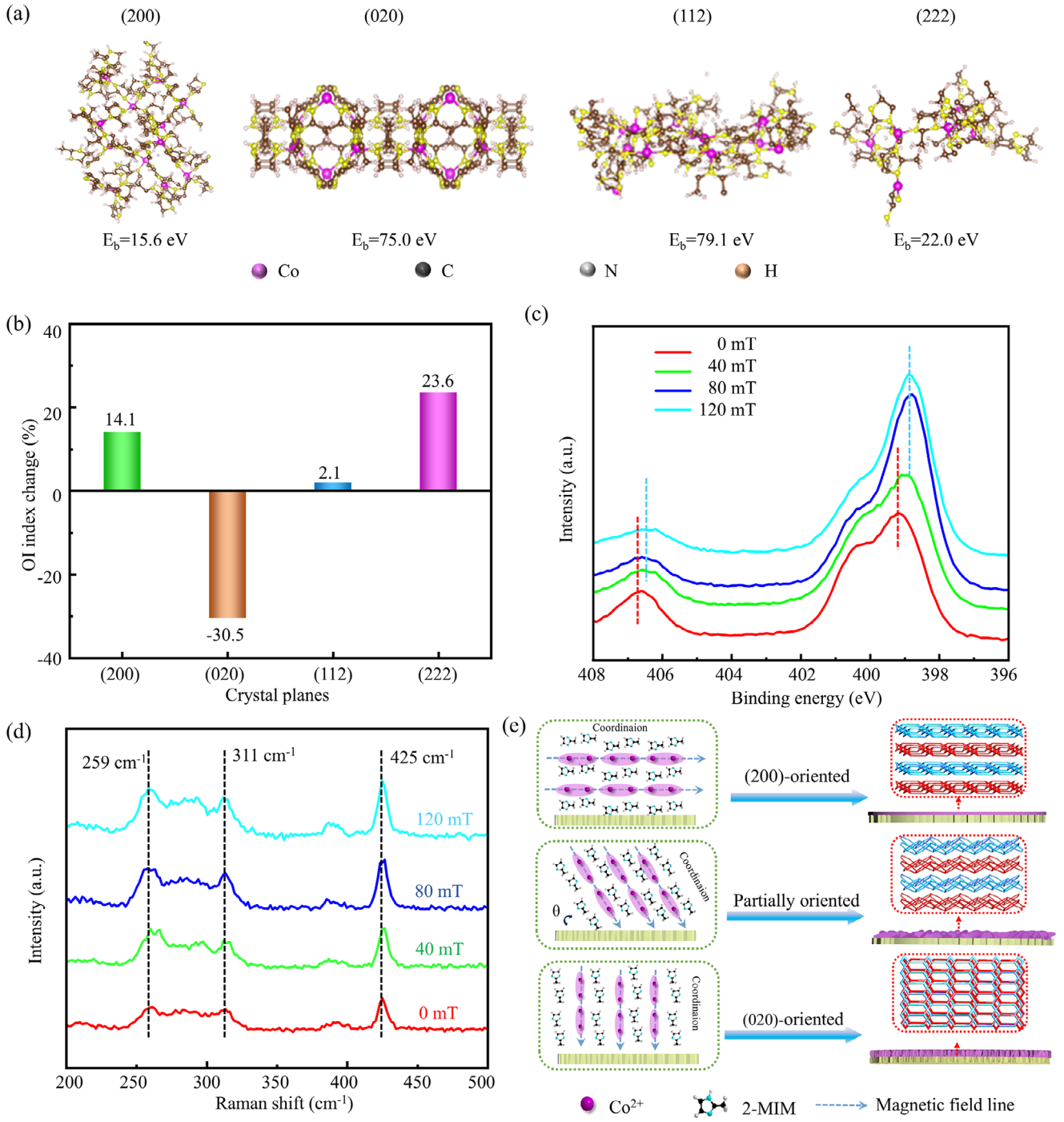

Figure 3. a) Structural models for different facets of Co-ZIF-L crystal. b) Changes in OI value, c) N 1s XPS spectra, and d) Raman spectra of Co-ZIF-L crystals prepared with different magnetic strengths. e) The diagram for the formation mechanism of Co-ZIF-L membranes.

magnetic anisotropy of Co-ZIF-L material. Thereby, ordered migration of Co^{2+} ions tends to coordinate along the easy magnetization direction of Co-ZIF-L grains, namely (200) direction, to reduce the surface energy, inducing the selective growth of MOF membranes. Therefore, the obtained Co-ZIF-L membranes always expose the (200) crystal plane (Figure 3e), no matter how the direction of the magnetic field lines changes, which explains the observations in Figures 1 and 2. This results in the preparation of MOF membranes with different orientations at room temperature and atmospheric pressure, overcoming the drawbacks of traditional preparation strategies that require high temperatures and pressures. This is beneficial for increasing the economy and safety of the membrane preparation process. Additionally, we have successfully prepared highly (011)- and (222)-oriented

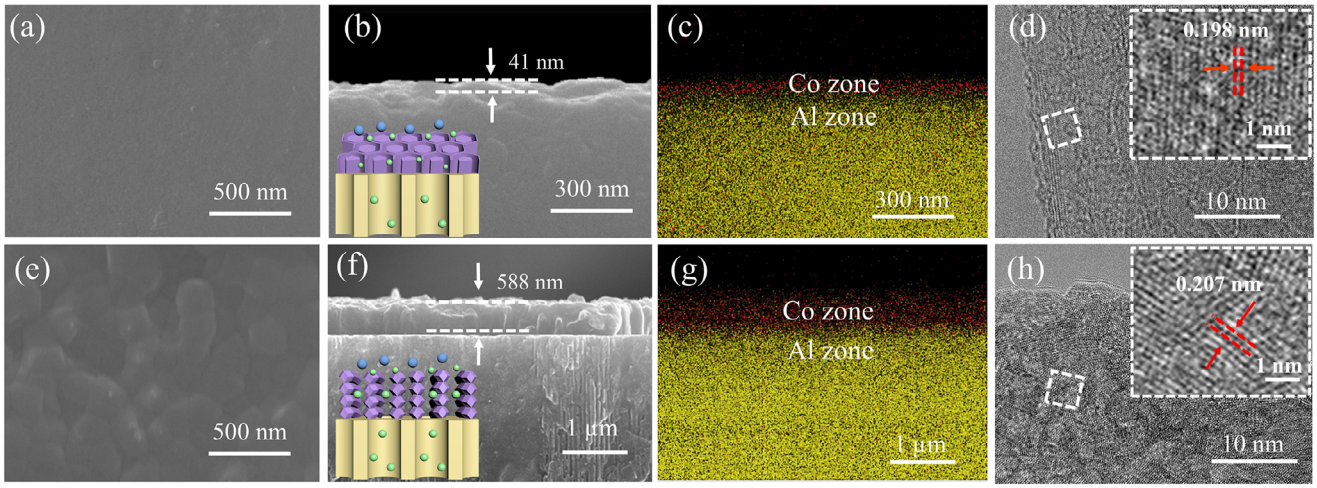

Figure 4. a) Surface view, b) cross-section view (inset: gas diffusion channels), c) EDS map, and d) TEM image (inset: HR-TEM) of (200)-oriented Co-ZIF-L membrane. e) Surface view, f) cross-section view ((inset: gas diffusion channels), g) EDS map, and h) TEM image (inset: HR-TEM) of (020)-oriented Co-ZIF-L membranes.

ZIF-67 membranes with this preparation principle, as shown in Figure S21 (Supporting Information). This reflects that the proposed strategy has definite expandability for developing oriented MOF membranes.

It is widely believed that highly oriented MOF membranes can reduce intergranular defects in the membrane and shorten the diffusion path of gas molecules, thereby simultaneously possessing high permeance and selectivity in the separation process. Therefore, key attentions are paid to highly (200)- and (020)-oriented Co-ZIF-L membranes. Their growth processes are shown in Figures S22 and S23 (Supporting Information), respectively, implying that the optimal synthesis time is 4 h. **Figure** 4a shows that (200)-oriented Co-ZIF-L membrane presents a continuous and dense surface with no obvious defects. From the cross-section SEM image (Figure 4b), a continuous MOF layer with a thickness of 41 nm is observed, providing hexagonal pores perpendicular to the AAO discs. The corresponding energy-dispersive X-ray spectroscopy (EDS) map in Figure 4c also confirms the successful construction of a Co-MOF membrane on the substrate. Then, transmission electron microscopy (TEM) analysis was performed, according to the work by Cui et al.[59] Figure 4d shows the TEM image of (200)-oriented Co-ZIF-L membrane, and the inserted high-resolution TEM (HR-TEM) shows that (200) crystal plane with a lattice spacing of 0.198 nm is dominant, indicating the oriented growth of MOF membranes. As for (020)-oriented Co-ZIF-L membranes, as shown in Figure 4e, the membrane surface is also continuous and defect-free; however, the surface is covered with MOF grains having distinct edges and corners, which is different from the (200)-oriented membrane; in addition, its thickness reaches 588 nm (Figure 4f), which is much thicker than the (200)-oriented counterpart, with a clear interface between different metal zones in EDS map (Figure 4g). The TEM result also confirms the predominance of (020) crystal plane (Figure 4h). This MOF membrane provides cushion-shaped channels with relatively large sizes,[60] which will contribute to improved gas separation performance.

Finally, gas separation performance of (020)-oriented and (200)-oriented MOF membranes was investigated, according to the pore characteristics of this MOF material and previous works on Zn-ZIF-L membranes.[35,36] As shown in **Figure** 5a,b, (200)-oriented Co-ZIF-L membrane delivers a H_2 permeance of 2872 GPU with ideal selectivity of 55.6, 44.7 and 72.3 for H_2/CO_2, H_2/N_2 and H_2/CH_4 gas pairs in single-gas separation measurement, respectively, which far exceed the corresponding Knudsen selectivity (4.7, 3.7 and 2.8), demonstrating the compactness of tested MOF membrane. The physical sieving of MOF pores plays a dominant role in the separation of H_2 and other gases based on their molecular dynamic diameter difference. The performance is superior to that of (020)-oriented Co-ZIF-L membrane in terms of both H_2 permeance and ideal selectivity, as shown in Figure S24 (Supporting Information). The (020)-oriented Co-ZIF-L membrane possesses a relatively larger aperture compared with that of (200)-oriented membrane; simultaneously, its relatively higher thickness increases gas diffusion resistance. So far as ideal selectivity is concerned, the smaller aperture of (200)-oriented Co-ZIF-L membrane exhibits higher sieving precision than (020)-oriented membrane, which is responsible for higher selectivity of the former. Higher H_2/CO_2 selectivity can also be attributed to higher affinity toward CO_2 over H_2, which stems from the interaction between uncoordinated nitrogen in free linkers and CO_2 molecules, rendering it promising for separating H_2/CO_2 mixture.[61]

Similarly, in terms of binary gas, as shown in Figure 5b and Figure S24 (Supporting Information), higher H_2 permeance as well as higher H_2/CH_4 and H_2/CO_2 separation factors can be observed for (200)-oriented MOF membrane. Figure 5b shows that H_2 permeance and H_2/CH_4 separation factor of Co-ZIF-L membrane reach 2275 GPU and 59.1, respectively, even though they have decreased compared with those in single gas permeation test due to competitive adsorption.[62] Subsequently, (200)-oriented Co-ZIF-L membrane was subjected to temperature-swing stability test for separating H_2/CH_4 mixtures, in which the operating temperature was increased from 30 to 150 °C, and

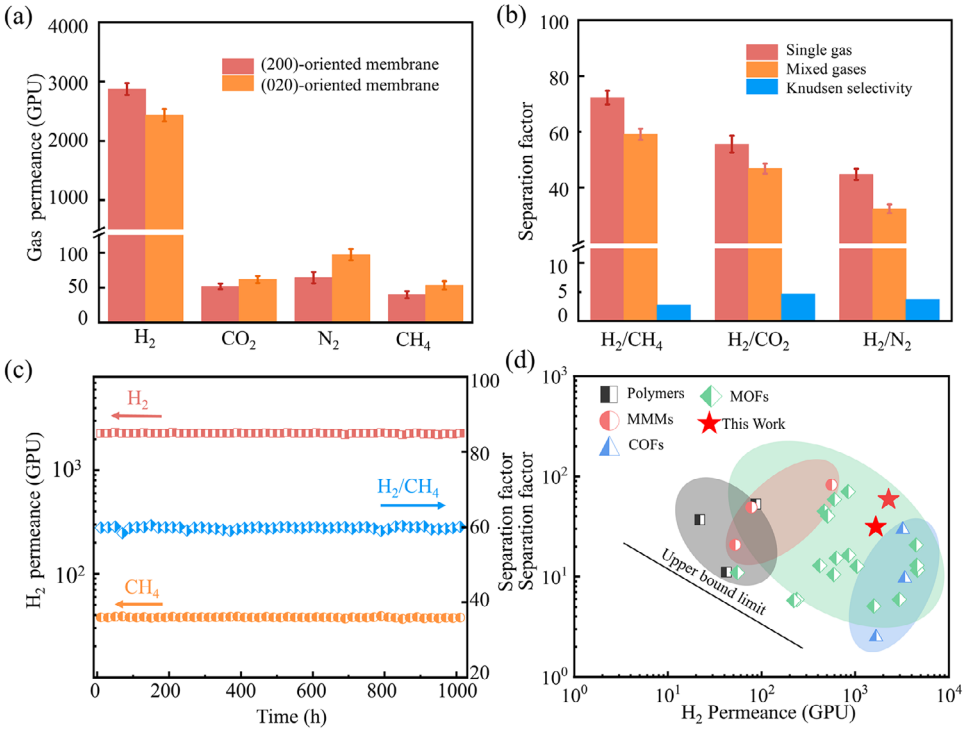

Figure 5. a) Single-gas separation performance. b) Separation selectivity and c) long-term stability for (200)-oriented Co-ZIF-L membranes. d) H_2/CH_4 separation performances of different membrane materials.

then decreased to 30 °C. As shown in Figure S25 (Supporting Information), its separation performance remains stable in the whole process; moreover, a high separation factor is still maintained under hyperthermic conditions, indicating huge potential for practical separations, which is attributed to the compensation effect for the adsorption enthalpy of activated permeation.[36] Under different operating pressures, the proposed membrane still exhibits minor performance change (Figure S26, Supporting Information), indicating its compactness. Additionally, the obtained MOF membranes also exhibit steady separation performance for 1000 h. It should be noted that the performance of the obtained Co-ZIF-L membrane not only goes beyond Robeson's upper bound (2008), but also is superior to the majority of reported membranes for H_2/CH_4 gas pair (Figure 5d; Table S1, Supporting Information) in terms of permeability. Regarding H_2/CO_2 separation, our membrane also exhibits outstanding performance concerning both H_2 permeances and H_2/CO_2 separator factor, as shown in Figure S27 and Table S2 (Supporting Information). The H_2/CO_2 performance of our Co-ZIF-L membrane is located within the US Department of Energy (DOE) target for CO_2 capture (H_2 permeance > 1000 GPU, H_2/CO_2 separation factor > 40),[63] thereby demonstrating great potential in practical pre-combustion-based carbon capture.

3. Conclusion

In summary, a magnetic-field assisted synthesis strategy is proposed to fabricate oriented Co-ZIF-L membranes, in which the membrane orientation can be precisely controlled by regulating the direction of the applied magnetic field. The mechanism studies indicated that the magnetic field would promote the rapid movement of Co^{2+} ions in specific directions, the easy magnetization axis of the Co-ZIF-L crystal, and enable the coordination along the (200) direction of MOF crystals to reduce the surface energy. This contributes to the directional growth and deposition of MOF membranes under different magnetic field directions. Specially, the obtained (200)-oriented Co-ZIF-L membrane, possessing an ultrathin thickness of about 40 nm, shows a high H_2 permeance of 2275 GPU and an impressive H_2/CH_4 separation factor of 59.1, belonging to one of the best-performing membranes for H_2/CH_4 separation. It is believed that this straightforward and gentle synthesis strategy will provide a powerful tool to prepare oriented MOF membranes for multitudinous critical separation challenges.

4. Experimental Section

Materials: Cobalt nitrate hexahydrate ($Co(NO_3)_2{\cdot}6H_2O$, 99%), 2-methylimidazole (2-MIM, 98%), and ethanol (99.5%) were supplied by Aladdin Biochemical Technology Co., Ltd. The chemicals were of direct use with no purification. AAO substrates (pore size: 80–100 nm, diameter: 25 mm) were supplied by Puyuan Nano Technology Co., Ltd, and Neodymium magnets were ordered in Shanghai Haoci Electromechanical Co., Ltd.

Fabrication of Co-ZIF-L Membranes: For preparing Co-ZIF-L membranes, 6.56 g $Co(NO_3)_2{\cdot}6H_2O$ and 2.91 g 2-MIM were dissolved in 25 mL homemade deionized (DI) water by magnetic stirring, respectively, followed by pouring the 2-MIM solution into the other solution. The AAO substrate was placed in a customized PTFE holder, and then was put in the above solution that was placed in a beaker. After that, two Neodymium magnets were placed on two sides of the beaker, and a uniform magnetic

field parallel to the AAO surface was generated, in which the magnetic field intensity was changed by adjusting the magnet number and the distance of the N and S poles. Besides, a TES1392 Tesla meter was adopted to detect magnetic field intensity. The membrane synthesis was performed under room temperature. After 4 h, the membrane-coated AAO disk was taken out and washed several times with DI water, followed by drying at 50 °C for 24 h. To create a magnetic field with different directions, the AAO disks were rotated around the vertical *z*-axis to varying degrees, and the angles (θ) between the magnetic field line and the AAO surface were changed accordingly (Figure S1, Supporting Information). In the case of a parallel magnetic field, θ was 0°, and the value was 90° when the magnetic field lines were vertically pointed to the AAO surface. Co-ZIF-L membranes were also synthesized under magnetic fields with different angles of θ = 15°, 30°, 45°, 60° and 75°, respectively, following the procedures shown above.

Characterizations: The morphology of prepared Co-ZIF-L membranes was observed on a field-emission SEM (Zeiss Sigma HD), accompanied by TEM analysis with a FEI TALOS-F200X instrument. The FT-IR spectroscopy was achieved on a Bruker Vertex70 FT-IR spectrophotometer, and a Thermo Scientific K-Alpha XPS system was used to detect the XPS spectra, with a LabRAM HR Evolution Raman spectrometer for the Raman spectra. Additionally, an investigation on the crystal phases of MOF membranes was conducted on a BRUKER D8 DISCOVER XRD. Orientation index (OI) was determined as follows:[40]

$$OI = \frac{I_{hkl,membrane}}{I_{hkl,standard}} \tag{1}$$

where IF_{hkl} represents the ratio of one certain diffraction peak to the sum of all characteristic peak intensities, as displayed in the following equation:[40]

$$IF_{hkl} = \frac{I_{hkl}}{I_{hkl} + I'_{hkl} + I''_{hkl}} \tag{2}$$

Electrochemical tests were conducted to explore the growth mechanism of oriented MOF membranes. Co^{2+} solutions were prepared by dissolving 6.56 g $Co(NO_3)_2{\cdot}6H_2O$ in 50 mL DI water. The conductivities of Co^{2+} solutions in magnetic fields with different intensities were detected using a DDS-307 conductivity meter with H-type cells.[64,65]

Theoretical Calculations: MS and DFT calculations were performed to assess the surface energy levels of different crystal planes for Co-ZIF-L. First, Co-ZIF-L unit cells of different crystal planes were geometrically optimized using the Forcite modules and COMPASS II in Materials Studio 2019, which were selected from the cif-file of CCDC 1 509 273. The Monkhorst-Pack grid was 3 × 3 × 3 with lattice parameters of x = 14.77 A°, y = 14.77 A°, z = 19.74 A°. The periodic boundary conditions were adopted in all three dimensions to ensure the simulation accuracy.[66] Geometric optimization of each structure was performed through energetic evaluation and conformational adjustment. Atomic coordinates and cell parameters were refined until the structure reached its minimum energy state.

DFT calculations were conducted in DMol^3 code of MS software, using the spin unrestricted method. The correlation effect and electron exchange were described by the generalized gradient approximation. A smearing value of 0.005 Ha was used for all calculations to the orbital occupation. The convergence tolerance for energy change, max force, and max displacement were 2.0×10^{-5} Ha, 0.004 Ha Å^{-1}, and 0.005 Å, respectively. A 3 ×3 ×1 Monkhorst-Pack grid was employed to execute the Brillouin-zone integrations. The surface energy at the crystal orientation was calculated as:[55]

$$\gamma = \frac{E_{slab} - E_{bulk} \times n}{2 \times A_{slab}} \tag{3}$$

where E_{slab} represents the total energy of the relaxed surface slab supercell, E_{bulk} represents the total energy of the original bulk crystal, n represents the ratio of the number of atoms of the relaxed surface slab supercell to the number of atoms of the original bulk crystal, and A_{slab} represents the surface area in the surface slab supercell.

Gas Permeation Measurements: (200)- and (020)-oriented Co-ZIF-L membranes were selected to test their gas separation performance on a home-made Wicke-Kallenbach setup (Figure S28, Supporting Information) after sealing them in a module with O-rings. The flow rate of feed gas was 50 mL min^{-1} in the single-gas permeation measurement with a transmembrane pressure of 1 bar. In the mixed-gas permeation tests, the mixture of H_2 and CO_2 or CH_4 (50/50 vol/vol) was delivered at a total flux of 50 mL min^{-1}, in which the transmembrane pressure was 1 bar. The permeate-side gas was blew in a gas chromatograph (Agilent 7890B) by Ar to analyze its composition. The gas permeance P_i was defined by the equation below:

$$P_i = \frac{N_i}{\Delta P_i \times A} \tag{4}$$

where N_i (mol s^{-1}), A (m^2), and ΔP_i (Pa) represent the molar flow rate of component *i*, the effective membrane area, and the transmembrane pressure difference, respectively.

The ideal selectivity ($a_{i/j}$) was described as follow: The ratio of permeance component i to j:

$$a_{i/j} = \frac{p_i}{p_j} \tag{5}$$

where P_i and P_j represent the permeance of component i and j, respectively.

The separation factor ($S_{i/j}$) was achieved with the following equation:

$$S_{i/j} = \frac{yi/yj}{xi/xj} \tag{6}$$

where $y_{(i,\,j)}$ and $x_{(i,\,j)}$ are the mole fractions of components (i, j) in the permeate and retentate, respectively.

Statistical Analysis: The error bars in Figure 5a,b and Figures S24 and S26 (Supporting Information) correspond to the standard deviations, which are achieved from three independent tests of corresponding membranes.

Supporting Information

Supporting Information is available from the Wiley Online Library or from the author.

Acknowledgements

F.J. Li and Z.Y. Cao contributed equally to this work. This study was subsidized by State Key Laboratory of Fine Chemicals, Dalian University of Technology (KF 2308), Post-graduate's Innovation Funding Project of Hebei Province (No. CXZZSS2024011), and National Natural Science Foundation of China (22278109).

Conflict of Interest

The authors declare no conflict of interest.

Data Availability Statement

The data that support the findings of this study are available from the corresponding author upon reasonable request.

Keywords

gas separation, magnetic field, MOF membranes, orientation regulation, ZIF-L

Received: September 25, 2025
Revised: November 11, 2025
Published online: November 22, 2025

[1] A. Knebel, J. Caro, *Nat. Nanotechnol.* **2022**, *17*, 911.
[2] S. Zhou, O. Shekhah, A. Ramírez, P. B. Lyu, J. T. J. E. A. Hamad, J. T. Li, P. M. Bhatt, Z. Y. Huang, H. Jiang, T. Jin, G. Maurin, J. Gascon, *Nature* **2022**, *606*, 706.
[3] H. Zhang, Z. H. Zhou, Y. N. Yin, H. Xu, Y. M. Wang, K. Yang, Z. J. Zhang, J. L. Wang, X. M. He, *EcoEnergy* **2023**, *1*, 217.
[4] T. Yan, J. H. Yang, J. M. Lu, L. Zhou, Y. Zhang, G. H. He, *J. Membr. Sci.* **2024**, *690*, 122225.
[5] C. Wang, T. T. Ji, Y. Y. Wu, G. H. He, Y. Liu, *ACS Mater. Lett.* **2023**, *5*, 1311.
[6] S. Zhou, O. Shekhah, J. T. Jia, J. Czaban-Jóźwiak, P. M. Bhatt, A. Ramírez, J. Gascon, M. Eddaoudi, *Nat. Energy* **2021**, *6*, 882.
[7] J. Y. Wang, Y. Wang, Y. T. Liu, H. Wu, M. G. Zhao, Y. X. Ren, Y. C. Pu, W. P. Li, S. Y. Wang, S. Q. Song, X. Liang, G. W. He, Y. Han, Z. Y. Jiang, *Adv. Funct. Mater.* **2022**, *32*, 2208064.
[8] B. Y. Mo, Y. H. Jin, G. Y. Zhou, G. Z. Liu, C. L. Chen, Z. K. Liu, G. P. Liu, W. Q. Jin, *AIChE J.* **2024**, *70*, 18368.
[9] X. Y. Wang, Y. N. Wang, F. C. Wu, G. F. Jin, J. D. Li, Z. S. Zhang, *Appl. Surf. Sci.* **2022**, *596*, 153628.
[10] Y. C. Wang, Y. J. Ban, Z. Y. Hu, W. S. Yang, *Nat. Commun.* **2023**, *14*, 6617.
[11] F. Dorosti, L. Ge, H. Wang, J. Bell, R. J. Lin, J. W. Hou, Z. H. Zhu, *Angew. Chem., Int. Ed.* **2025**, *137*, 202417513.
[12] Y. W. Sun, J. H. Yan, Y. L. Gao, T. T. Ji, S. X. Chen, C. Wang, P. Lu, Y. S. Li, Y. Liu, *Angew. Chem., Int. Ed.* **2023**, *62*, 20221669.
[13] Q. Wu, Y. Jiao, L. Liu, Y. Sun, T. L. Han, Y. Peng, W. S. Yang, S. J. Luo, S. J. Zhang, *Chem. Eng. J.* **2023**, *461*, 141976.
[14] I. E. Khalil, J. Fonseca, M. R. Reithofer, T. Eder, J. M. Chin, *Coord. Chem. Rev.* **2023**, *481*, 215043.
[15] R. C. Wei, X. W. Liu, Z. Y. Zhou, C. L. Chen, Y. Y. Yuan, Z. Li, X. Li, X. L. Dong, D. W. Lu, Y. Han, Z. P. Lai, *Sci. Adv.* **2022**, *8*, abm6741.
[16] Y. W. Sun, Y. Liu, *Chem. - Eur. J.* **2024**, *30*, 202304162.
[17] J. Xu, R. X. Wang, H. Q. Jiang, X. T. Liu, L. C. An, S. Y. Jin, B. W. Deng, W. Z. Wu, G. J. Cheng, *Adv. Sci.* **2021**, *8*, 2102477.
[18] K. Zhu, Y. M. Ju, J. J. Xu, Z. Y. Yang, S. Gao, Y. L. Hou, *Acc. Chem. Res.* **2018**, *51*, 404.
[19] Y. Qian, D. M. Wang, X. F. Tian, H. J. Liu, X. Y. Wang, H. Li, Q. W. Chen, X. Zhang, H. Wang, *Chem. Eng. J.* **2020**, *400*, 125823.
[20] L. Hu, R. R. Zhang, Q. W. Chen, *Nanoscale* **2014**, *6*, 14064.
[21] I. Dobosz, D. Kutyła, M. Kac, G. Włoch, P. Zabinski, *Mater. Sci. Eng. B* **2020**, *262*, 114795.
[22] Y. Y. Wei, L. Ying, X. H. Ma, L. Zhou, Z. F. Zi, J. M. Dai, *J. Alloys Compd.* **2022**, *926*, 166774.
[23] C. Kim, Y. Yang, D. H. Lopez, *J. Electrochem. Soc.* **2021**, *168*, 040502.
[24] J. Zhou, D. Y. Zhang, G. H. Sun, C. K. Chang, *Solid State Ionics* **2019**, *338*, 96.
[25] X. Lyu, W. N. Zhang, S. Liu, X. Y. Wang, G. Li, B. W. Shi, K. Wang, X. Wang, Q. Wang, Y. Jia, *J. Energy Chem.* **2021**, *53*, 192.
[26] S. K. Wang, S. Wu, Y. C. Song, H. Gomaa, C. H. An, Q.-B. Deng, N. Hu, *Rare Met.* **2024**, *43*, 2391.
[27] J. B. Chen, J. Ying, Y. Tian, Y. X. Xiao, X. Y. Yang, *Adv. Funct. Mater.* **2025**, *8*, 2415660.
[28] X. J. Zeng, W. Zhou, P. Z. Zhou, M. Zhang, C. L. Zhou, L. X. Tan, J. Environ, L. Wang, *Chem. Eng.* **2021**, *9*, 105325.
[29] Y. Liu, C. Wu, Z. M. Zhou, W. Liu, H. Y. Guo, B. Q. Zhang, *J. Membr. Sci.* **2022**, *659*, 120787.
[30] H. Li, J. W. Hou, T. D. Bennett, J. D. Liu, Y. T. Zhang, *J. Mater. Chem. A* **2019**, *7*, 5811.
[31] K. Yang, S. L. Hu, Y. J. Ban, Y. W. Zhou, N. Cao, M. Zhao, Y. F. Xiao, W. X. Li, W. S. Yang, *Sci. Bull.* **2021**, *66*, 1869.
[32] J. Y. Zhu, H. Li, J. W. Hou, J. D. Liu, Y. T. Zhang, B. V. Bruggen, *AIChE J.* **2020**, *66*, 16935.
[33] Q. Q. Hou, S. Zhou, Y. Y. Wei, J. Caro, H. H. Wang, *J. Am. Chem. Soc.* **2020**, *142*, 9582.
[34] L. H. Xu, S. H. Li, H. Mao, Y. Li, A. S. Zhang, S. Wang, W. M. Liu, J. Lv, T. Wang, W. W. Cai, L. Sang, W. W. Xie, C. Pei, Z. Z. Li, Y. N. Feng, Z. P. Zhao, *Science* **2022**, *378*, 308.
[35] Z. X. Zhong, J. F. Yao, R. Z. Chen, Z. X. Low, M. He, J. Z. Liu, H. T. Wang, *J. Mater. Chem. A* **2015**, *3*, 15715.
[36] Y. Y. Liang, C. J. Yu, J. G. Ju, Z. H. Qiao, C. L. Zhong, *Sci. Bull.* **2020**, *65*, 1788.
[37] P. Cheng, Y. D. Huang, C. Wu, X. P. Wang, X. R. Fu, P. Li, Y. L. Liu, S. J. Xia, *J. Membr. Sci.* **2021**, *640*, 119812.
[38] Q. Q. Hou, Y. Wu, S. Zhou, Y. Y. Wei, J. Caro, H. H. Wang, *Angew. Chem., Int. Ed.* **2019**, *58*, 327.
[39] J. L. Han, H. Y. Wu, H. W. Fan, L. Ding, G. T. Hai, J. Caro, H. H. Wang, *J. Am. Chem. Soc.* **2023**, *145*, 14793.
[40] Y. X. Sun, F. Yang, Q. Wei, N. X. Wang, X. Qin, S. K. Zhang, B. Wang, Z. R. Nie, S. L. Ji, H. Yan, J. R. Li, *Adv. Mater.* **2016**, *28*, 2374.
[41] Z. W. Zheng, M. H. Xia, X. Y. Chen, X. Xiao, J. W. Gong, J. L. Liu, J. K. Du, Y. R. Tao, Y. Hu, A. Y. Mei, X. H. Lu, H. W. Ha, *Adv. Energy Mater.* **2023**, *13*, 2204335.
[42] Y. Z. Wang, T. Sun, A. H. B. Mostaghimi, T. J. Goncalves, Z. Z. Liang, Y. Y. Zhou, W. Zhang, Z. H. Huang, Y. H. Ma, R. Cao, S. Siahrostami, H. Q. Zheng, *CCS Chem.* **2022**, *4*, 1633.
[43] Q. Xu, Y. Y. Sun, Z. Y. Tan, W. J. Guo, F. J. Li, X. R. Hou, Y. Guo, F. C. Wu, *J. Membr. Sci.* **2025**, *726*, 124077.
[44] W. J. Zhang, J. G. Gao, Y. L. Huang, G. G. Xu, Y. Chen, G. Y. Zhao, Y. B. Lin, Z. G. Huang, J. X. Li, *Adv. Funct. Mater.* **2023**, *33*, 230635.
[45] Z. Yu, D. Zhang, Y. Wang, F. Liu, F. She, J. Chen, Y. Zhang, R. Wang, Z. Zeng, L. Song, *Adv. Mater.* **2024**, *36*, 2408461.
[46] Y. W. Sun, H. Lv, H. Yao, Y. F. Gao, C. M. Zhang, *Carbon Energy* **2024**, *6*, 575.
[47] Y. Y. Wei, L. Ying, X. H. Ma, L. Zhou, Z. F. Zia, J. M. Dai, *J. Alloys Compd.* **2022**, *926*, 166774.
[48] C. Kim, Y. Yang, D. H. Lopez, *J. Electrochem. Soc.* **2021**, *168*, 040502.
[49] C. Kim, Y. Yang, D. H. Lopez, D. Ha, *Appl. Phys. Lett.* **2020**, *117*, 123903.
[50] L. Zhang, M. Y. Zeng, D. D. Wu, X. B. Yan, *ACS Sustainable Chem. Eng.* **2019**, *7*, 6152.
[51] C. Y. Zhang, C. Q. Zhang, G. W. Sun, J. L. Pan, L. Gong, G. Z. Sun, J. J. Biendicho, L. Balcells, X. L. Fan, J. R. Morante, J. Y. Zhou, A. Cabot, *Angew. Chem., Int. Ed.* **2022**, *61*, 202211570.
[52] G. Zhou, P. Wang, H. Li, B. Hu, Y. Sun, R. Huang, L. Liu, *Nat. Commun.* **2024**, *12*, 4827.
[53] F. J. Li, H. Zhang, F. C. Wu, X. R. Hou, Q. Xu, J. D. Li, Y. Guo, Z. Y. Jiang, *Adv. Funct. Mater.* **2025**, *22*, 2422400.
[54] R. S. M. Rikken, R. J. M. Nolte, J. C. Maan, J. C. M. van Hest, D. A. Wilson, P. C. M. Christianen, *Soft Matter* **2014**, *10*, 1295.
[55] B. Motevalli, N. Taherifar, H. T. Wang, J. Z. Liu, *J. Phys. Chem. C* **2017**, *121*, 2221.
[56] S. C. Hui, Q. Chen, K. Tao, L. M. Zhang, X. M. Fan, R. C. Che, H. J. Wu, *Adv. Mater.* **2025**, *37*, 2415844.
[57] D. C. Gao, J. X. Yang, D. Y. n Zhang, C. K. Chang, *Ceram. Int.* **2022**, *48*, 31598.

[58] M.-P. Jiang, K. K. Huang, J. H. Liu, D. Wang, Y. Wang, X. Wang, Z. D. Li, X. Y. Wang, Z. B. Geng, X. Y. Hou, S. H. Feng, *Chem* **2020**, *6*, 2335.
[59] M. Y. Cui, Y. Wei, S. C. Hui, T. Zhang, G. Chen, Y. Zhang, Z. G. Gao, J. Q. Zhang, H. J. Wu, *Adv. Funct. Mater.* **2025**, *35*, 2508939.
[60] S. S. Wang, J. T. Liu, B. Pulido, Y. F. Li, D. Mahalingam, S. P. Nunes, *ACS Appl. Nano Mater.* **2020**, *3*, 3839.
[61] R. Z. Chen, J. F. Yao, Q. F. Gu, S. Smeets, C. Baerlocher, H. X. Gu, D. R. Zhu, W. Morris, O. M. Yaghi, H. T. Wang, *Chem. Commun.* **2013**, *49*, 9500.
[62] Z. H. Qiao, Y. Y. Liang, Z. Q. Zhang, D. H. Mei, Z. Wang, M. D. Guiver, C. L. Zhong, *Adv. Mater.* **2020**, *32*, 2002165.
[63] M. Luo, Z. Lu, Y. L. Zhao, Y. F. Wang, Y. Y. Wei, H. H. Wang, *AIChE J.* **2023**, *69*, 18105.
[64] P. W. Majewski, M. Gopinadhan, W. S. Jang, J. L. Lutkenhaus, C. O. Osuji, *J. Am. Chem. Soc.* **2010**, *132*, 17516.
[65] P. Z. Sun, F. Zheng, K. L. Wang, M. L. Zhong, D. H. Wu, H. W. Zhu, *Sci. Rep.* **2014**, *4*, 6798.
[66] M. Sadeghi, F. Esmaeilzadeh, D. Mowla, A. Zandifar, *Sep. Purif. Technol.* **2024**, *338*, 126534.